ORIGINAL ARTICLE

Simple Synthesis and Thermoelectric Properties of $Mg_{2+x}Si_{0.5}Sn_{0.5}Sb_{0.075}$ Materials with Heterogeneous Microstructure

Jeongin Jang[1] · Bok-Ki Min[1] · Bong-Seo Kim[1] · Sung-Jae Joo[1] · Yong Il Park[2] · Ji Eun Lee[2]

Abstract

Mg_2X (X = Si, Ge or Sn) based alloys are considered as promising candidates in the middle to high temperature range thermoelectric applications due to their low cost, nontoxicity and abundance of constituent elements. However, they exhibit relatively higher thermal conductivity compared to other thermoelectric materials. In this study, we present a simple synthetic method for a $Mg_{2+x}Si_{0.5}Sn_{0.5}Sb_{0.075}$ material with a heterogeneous microstructure that reduces thermal conductivity. By controlling the amount of excess Mg during synthesis, a heterogeneous microstructure due to the formation of secondary phases was obtained. This heterogeneous microstructure reduced the thermal conductivity through phonon scattering, leading to an improved thermoelectric efficiency, particularly at high temperatures.

Keywords Thermoelectric · Lattice thermal conductivity · Magnesium silicide · Heterogeneous microstructure · Phonon scattering

Introduction

The increasing energy consumption and environmental pollution caused by fossil fuels have encouraged research on energy harvesting technologies [1], including thermoelectric generation. As only 30–40% of fossil fuels are utilized as useful energy in heat engines and the rest is wasted as heat, thermoelectric materials, which can directly convert waste heat into electrical energy, have been attracting considerable interest [2–4]. However, environmental issues related to heavy metals and the high cost of key elements in high-performance thermoelectric materials such as Bi–Te and Pb–Te render their practical use difficult [5].

On the other hand, among thermoelectric materials, Mg_2X (X = Si, Ge, or Sn)-based alloys are considered promising candidates for moderate-to-high-temperature

applications owing to their low cost, their nontoxicity, and abundance of their constituent elements [6–11]. Cost-effective and environmentally friendly Mg_2X materials have the potential for use in large-scale commercial thermoelectric power generators. Furthermore, they have a high-power output per unit mass compared to other thermoelectric materials, which could lead to future applications in mobility.

A material's thermoelectric efficiency can be estimated from the figure of merit ZT ($= S^2\sigma T/\kappa$, where S is the Seebeck coefficient, σ is the electrical conductivity, T is the absolute temperature, and κ is the thermal conductivity). Thus, to have a high thermoelectric efficiency, a thermoelectric material should have a low thermal conductivity and a high electrical conductivity [12, 13]. In particular, Mg_2X-based alloys (6–8 W/mK) have relatively higher thermal conductivity than other thermoelectric materials [14, 15]. Hence, strategies for reducing the thermal conductivity have been intensively researched. For example, forming a solid solution of Mg_2Si and Mg_2Sn can significantly reduce the thermal conductivity owing to enhanced point defect phonon scattering [15]. Furthermore, dopants such as Sb, Bi, and Al, which induce n-type conductivity, and Ga, Li, and Ag, which induce p-type conductivity, enhance phonon scattering and thereby reduce the lattice thermal conductivity [16–22].

✉ Yong Il Park
 ypark@jnu.ac.kr

✉ Ji Eun Lee
 jelee@jnu.ac.kr

1 Energy Conversion Research Center, Korea Electrotechnology Research Institute, Changwon 51543, South Korea

2 School of Chemical Engineering, Chonnam National University, Gwangju 61186, South Korea

Here we report a straightforward synthesis of $Mg_{2+x}Si_{0.5}Sn_{0.5}Sb_{0.075}$ ($x = 0.05$, 0.10, 0.15, and 0.20) materials with a heterogeneous microstructure resulting from formation of secondary phase, and investigate the effect of this heterogeneous microstructure on the thermoelectric properties of the material. In the typical synthesis of Mg_2X materials using the solid-state reaction method, an excess amount of Mg, approximately 10% above the stoichiometric ratio, is added to compensate for its high vapor pressure and potential loss during synthesis [10, 22, 23]. However, in this study, unlike the conventional approach, $Mg_{2+x}Si_{0.5}Sn_{0.5}Sb_{0.075}$ was synthesized with a reduced amount of excess Mg, resulting in the formation of Sn-rich secondary phases within the solid solution. By simply reducing the excess Mg content, a heterogeneous microstructure can be obtained, leading to a decrease in thermal conductivity due to phonon scattering and an enhancement in thermoelectric efficiency, particularly at high temperatures. This result demonstrates that the microstructure can be controlled by adjusting the excess Mg content during synthesis, and shows that this microstructure affects the thermoelectric performance.

Experimental Procedures

$Mg_{2+x}Si_{0.5}Sn_{0.5}Sb_{0.075}$ ($x = 0.05$, 0.10, 0.15, and 0.20) compounds were prepared through a solid-state reaction. Commercial high-purity powders of Mg (99.6%), Si (99.9985%), Sn (99.995%), and Sb (99.999%) were used in stoichiometric quantities. The raw materials were mixed homogeneously, and they were then cold-pressed under a pressure of 300 MPa to form pellets. The pellets were sealed in quartz tubes in an Ar atmosphere, and the tube was heated to a temperature of 923 K and maintained at the temperature for 24 h. The synthesized compounds were ground into powders. Fine powders were obtained through sieving and spark plasma sintering in a cylindrical graphite mold with an internal diameter of 12.7 mm at 1003 K under a pressure of 50 MPa for 15 min in an Ar atmosphere. The fine powders were heat-treated at 823 K for 24 h to stabilize the phase. The densities of the sample were determined using the Archimedes method, and they were found to be above 98%. The crystalline phases were analyzed using X-ray diffraction (X'Pert PRO, PANalytical) with Cu Kα radiation. The spark plasma sintered samples were cut to a rectangular shape with dimensions of 3 mm × 3 mm × 12 mm for electrical resistivity and Seebeck coefficient measurements, and to a disc shape with dimensions of 12.7 mm (diameter) × 2 mm (thickness) for thermal diffusivity measurements. The Seebeck coefficient and electrical resistivity were measured from *RT* to 823 K at intervals of 50 K by using ZEM-3 (ULVAC-RIKO), the thermal diffusivity was measured using a thermal analyzer (LFA 457, Netzsch), and the thermal

conductivity was calculated using the formula $\kappa = \alpha \gamma C_p$, where α is the thermal diffusivity, γ is the density, and C_p is the specific heat of the material. Previously reported C_p data for Mg_2Si were used [24].

Results and Discussion

X-ray diffraction patterns of $Mg_{2+x}Si_{0.5}Sn_{0.5}Sb_{0.075}$ samples prepared with different Mg content ($x = 0.05$, 0.10, 0.15 and 0.20) are shown in Fig. 1. All major diffraction peaks are located between those of pure Mg_2Si and Mg_2Sn and can be indexed to the face-centered cubic antifluorite structure with the *Fm3m* space group, indicating the formation of a solid solution without unreacted free Mg, Si, or Sn. The diffraction peaks around $2\theta = 23°$, 38°, 45°, and 56°, which correspond to the (1 1 1), (2 2 0), (3 1 1), and (4 0 0) planes, appear as a single peak for the $x = 0.2$ sample with sufficiently excess Mg. However, for other samples with low Mg content, secondary peaks appear at lower 2θ values, and the intensities of the peaks increase as the Mg content decreases. These secondary peaks indicate the existence of another composition, and on the basis of the atom sizes of Sn and Si (radii of 145 pm for Sn and 118 pm for Si), they appear to correspond to an Sn-rich secondary phase.

Microstructural images of the $Mg_{2.2}Si_{0.5}Sn_{0.5}Sb_{0.075}$ and $Mg_{2.05}Si_{0.5}Sn_{0.5}Sb_{0.075}$ samples are shown in Fig. 2. A backscattered electron (BSE) image of the $Mg_{2.2}Si_{0.5}Sn_{0.5}Sb_{0.075}$ sample in Fig. 2a shows grey grains that have a mosaic-like structure and that are several microns in size. Electron
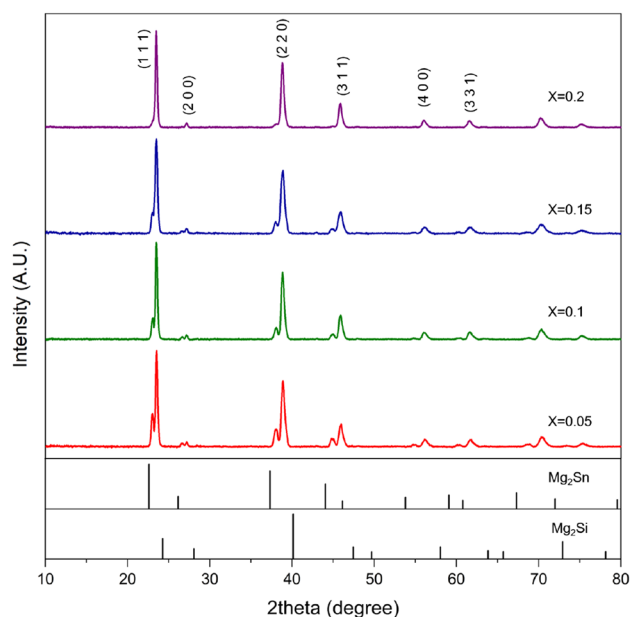
Fig. 1 XRD patterns of $Mg_{2+x}Si_{0.5}Sn_{0.5}Sb_{0.075}$ ($x = 0.05$, 0.10, 0.15, and 0.20) samples with different Mg contents

Fig. 2 BSE images of **a** $Mg_{2.2}Si_{0.5}Sn_{0.5}Sb_{0.075}$ and **b** $Mg_{2.05}Si_{0.5}Sn_{0.5}Sb_{0.075}$
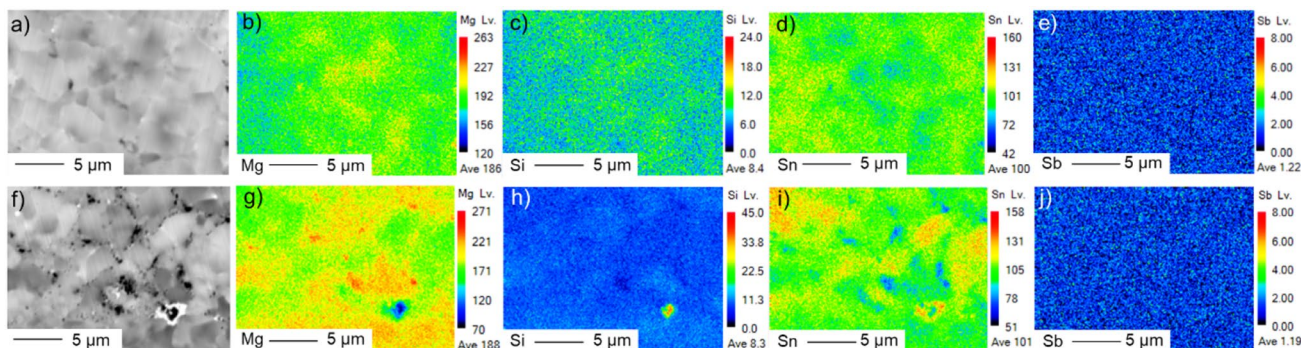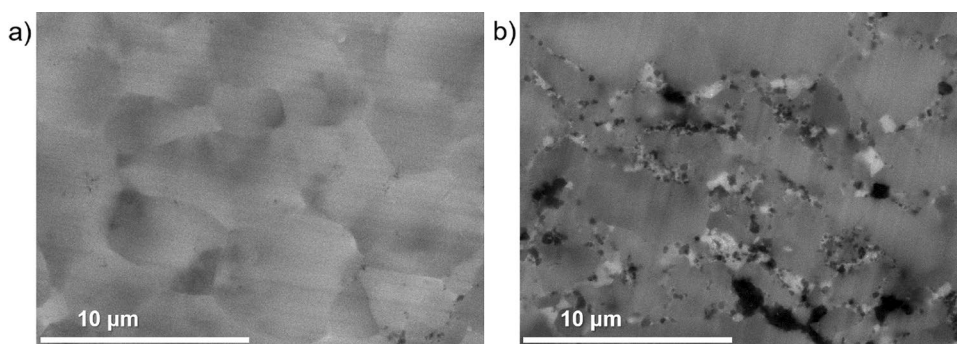
Fig. 3 **a**, **f** BSE and **b–e**, **g–j** EPMA elemental mapping images of **a–e** $Mg_{2.2}Si_{0.5}Sn_{0.5}Sb_{0.075}$ and **f–j** $Mg_{2.05}Si_{0.5}Sn_{0.5}Sb_{0.075}$

probe micro-analyzer (EPMA) elemental mapping images (Fig. 3b–e) showed that Mg, Sn, Si, and Sb were relatively evenly distributed and that the grains had homogeneous composition. On the other hand, for $Mg_{2.05}Si_{0.5}Sn_{0.5}Sb_{0.075}$, whose Mg content was lower, a BSE image (Fig. 2b) showed that its microstructure differed from that of the $Mg_{2.2}Si_{0.5}Sn_{0.5}Sb_{0.075}$ sample (with sufficiently excessive Mg content). In Fig. 2b, many light and dark spots are apparent between the grey grains, indicating the presence of other phases with different compositions. The elemental mapping images of $Mg_{2.05}Si_{0.5}Sn_{0.5}Sb_{0.075}$ in Fig. 3g–j shows that the distribution of elements was not uniform and that the dark spots in the BSE image of Fig. 2b had high Mg content and lacked Sn while the bright areas had high Sn content. Considering the XRD plot of Fig. 1, we can see that the Sn-rich phase of the bright part in elemental mapping images is consistent with the secondary peaks at low 2θ values. Both the element mapping images and XRD plot show that the uniformity of composition decreased and phase separation occurred when a lower amount of Mg was used. These results demonstrate that the phase of materials can be controlled by simple tuning of elemental composition [25]. In the case of Mg_2X-based alloys, phase stability can be changed and phase separation can be induced by doping elements such as Sb or Bi or changing the composition of the constituent elements [8, 26–29]. EDS elemental analysis for a wide area (Table 1) allows us to estimate the

Table 1 EDS elemental analysis for a wide area of the $Mg_{2+x}Si_{0.5}Sn_{0.5}Sb_{0.075}$ samples (the Sb composition ratio is represented as 0.0075 due to the small amount that is difficult to detect)

Nominal composition ($Mg_{2+x}Si_{0.5}Sn_{0.5}Sb_{0.075}$)	EDS composition
$x=0.05$	$Mg_{1.956}Si_{0.605}Sn_{0.439}Sb_{0.075}$
$x=0.10$	$Mg_{1.961}Si_{0.552}Sn_{0.488}Sb_{0.075}$
$x=0.15$	$Mg_{1.978}Si_{0.523}Sn_{0.499}Sb_{0.075}$
$x=0.20$	$Mg_{2.015}Si_{0.500}Sn_{0.485}Sb_{0.075}$

overall composition of the $Mg_{2+x}Si_{0.5}Sn_{0.5}Sb_{0.075}$ samples, revealing magnesium deficiency below stoichiometric levels, except in the case of $x=0.2$. This observation aligns with a recent report that a deficiency in magnesium leads to phase separation [28]. Furthermore, our experimental outcomes demonstrate that a slight adjustment in elemental composition, specifically the magnesium content, influences not only phase separation but also microstructural changes.

To investigate the effect of the heterogeneous microstructure on the thermoelectric performance, we determined the temperature dependence of the thermoelectric properties of the samples. The electrical conductivities in Fig. 4a show that samples with sufficient amounts of Mg had low electrical conductivities over the entire temperature range. The difference in electrical conductivity was not significant, but the lower the amount of Mg, the higher the electrical conductivity. Figure 4b
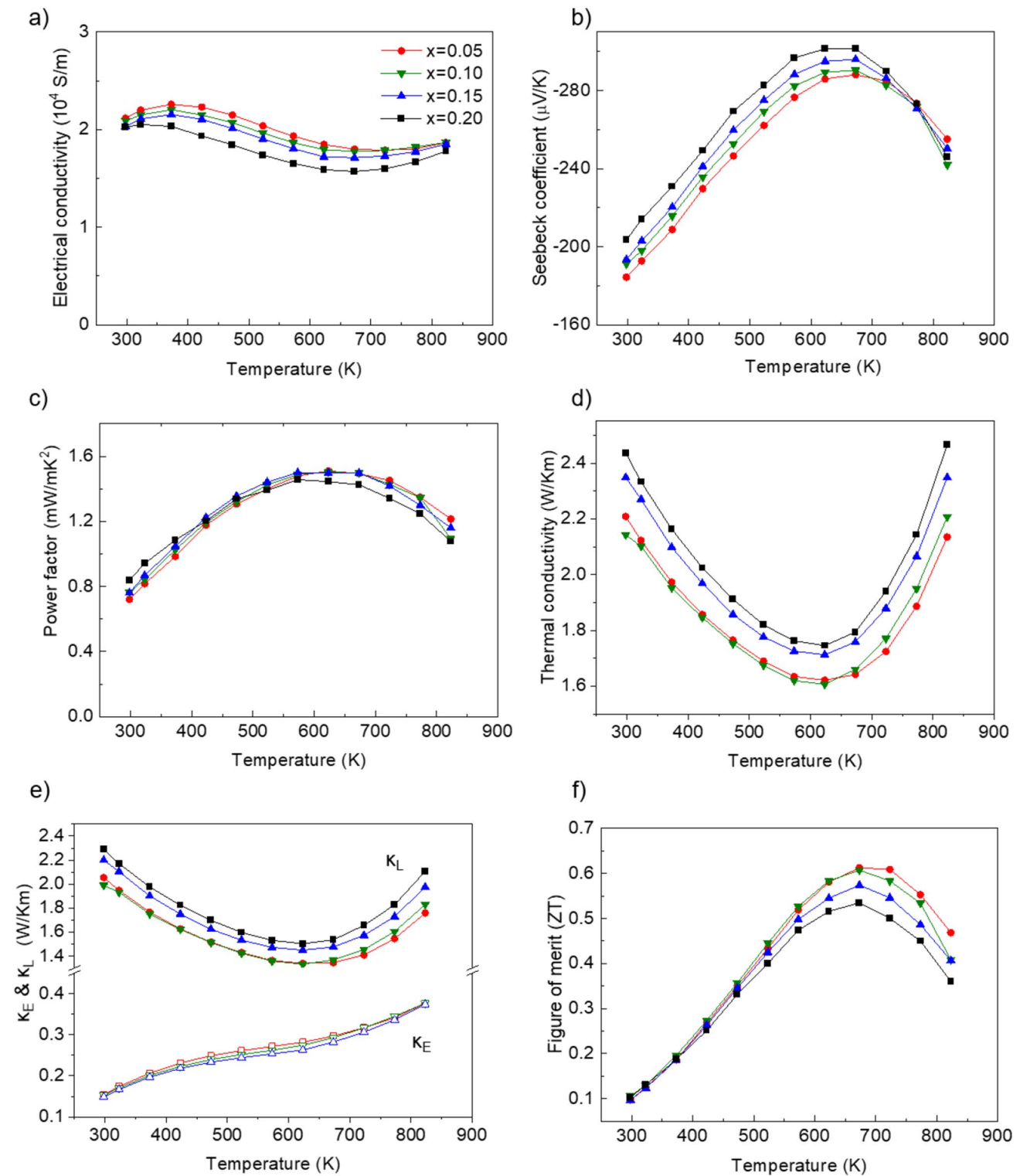
Fig. 4 Thermoelectric properties of $Mg_{2+x}Si_{0.5}Sn_{0.5}Sb_{0.075}$ materials. **a** Electrical conductivity, **b** Seebeck coefficient, **c** power factor, **d** thermal conductivity, **e** electronic thermal conductivity (κ_E) and lattice thermal conductivity (κ_L) and **f** ZT value as functions of temperature

shows the Seebeck coefficient as a function of the temperature for all the samples. All the samples exhibited negative Seebeck coefficients because of the n-type doping effect of Sb.

In contrast to the electrical conductivity, the absolute value of the Seebeck coefficient increased with the amount of Mg for temperatures below 773 K. Consequently, the power factor,

which was calculated using the equation $PF = S^2\sigma$ and which is shown in Fig. 4c, was similar for all samples over the entire temperature range. Although samples with a sufficient amount of Mg had slightly higher values in the low-temperature region and samples with a small amount of Mg had slightly higher values in the high-temperature region, the difference was not significant.

However, unlike the electrical properties of the samples, which did not differ significantly between samples with different Mg content, the thermal properties showed a pronounced difference. Figure 4d shows that the thermal conductivity of a sample with a small amount of Mg was lower than that of a sample with a sufficiently large amount of Mg. The figure also shows that below 623 K, the thermal conductivity of all samples decreased with an increase in the temperature, and that above this temperature, the thermal conductivity increased with the temperature.

Thermal conductivity comprises two components: electronic thermal conductivity κ_E, and lattice thermal conductivity κ_L. These two components are associated with charge carriers and phonons, respectively. The electronic thermal conductivity can be estimated in terms of the electrical conductivity σ by using the Wiedemann–Franz law: $\kappa_E = LT\sigma$, where L is the Lorenz number and T is the temperature in kelvin [30, 31]. The lattice thermal conductivity κ_L is obtained by subtracting the electronic thermal conductivity κ_E from the thermal conductivity. Figure 4e, which depicts the calculated κ_E and κ_L, shows that the decrease in the thermal conductivity of the sample with a small amount of Mg resulted from a decrease in the lattice thermal conductivity. This decrease in the lattice thermal conductivity is considered to have been caused by the nonuniform microstructure associated with the Sn-rich phase. Heterogeneous microstructures such as those of nano inclusions and nanoparticles are known to reduce the lattice thermal conductivity [32–34], and they can form many interfaces. In thermoelectric materials, phonons that transfer heat are scattered by these interfaces, and hence, the materials have a low thermal conductivity and a high thermoelectric conversion efficiency. The decrease in the thermal conductivity due to phonon scattering and the resulting improvement in thermoelectric properties are consistent with our result [23, 35]. In fact, it is apparent in Fig. 4f that the sample with a small amount of Mg and an Sn-rich heterogeneous microstructure showed a reduced lattice thermal conductivity and hence an improved ZT value, especially at high temperatures.

Conclusions

In summary, this study reveals that the internal microstructure of $Mg_{2+x}Si_{0.5}Sn_{0.5}Sb_{0.075}$ material is influenced by the amount of excess Mg used during synthesis. When the sample was synthesized with a sufficient excess of Mg ($x = 0.2$), a homogeneous microstructure was observed. However, as the amount of Mg decreases, a Sn-rich phase appears, leading to a heterogeneous microstructure. The presence of heterostructures reduces lattice thermal conductivity through phonon scattering at phase boundaries, leading to an increase in the ZT value at higher temperatures. These findings not only contribute to the development of a simple method for synthesizing heterogeneous $Mg_{2+x}Si_{0.5}Sn_{0.5}Sb_{0.075}$ material but also underscore the importance of controlling the microstructure to optimize the thermoelectric properties of the material.

Declarations

References

1. V.I. Manousiouthakis, S.H. Choi, Korean J. Chem. Eng. **38**, 2003 (2021)
2. X.-L. Shi, J. Zou, Z.-G. Chen, Chem. Rev. **120**, 7399 (2020)
3. M.A. Zoui, S. Bentouba, J.G. Stocholm, M. Bourouis, Energies (Basel). **13**, 3606 (2020)
4. H.J. Im, B. Koo, M.-S. Kim, J.E. Lee, Korean J. Chem. Eng. **39**, 1227 (2022)
5. S. Leblanc, S.K. Yee, M.L. Scullin, C. Dames, K.E. Goodson, Renew. Sustain. Energy Rev. **32**, 313 (2014)
6. M.B.A. Bashir, S. Mohd Said, M.F.M. Sabri, D.A. Shnawah, M.H. Elsheikh, Renew. Sustain. Energy Rev. **37**, 569 (2014)
7. W. Liu, K. Yin, Q. Zhang, C. Uher, X. Tang, Natl. Sci. Rev. **4**, 611 (2017)
8. J. Jang, B. Ryu, S.-J. Joo, B.-S. Kim, B.-K. Min, H.-W. Lee, S.-D. Park, H.S. Lee, J.E. Lee, J. Alloys Compd. **739**, 129 (2018)
9. J. Camut, N.H. Pham, D.Y. Nhi Truong, G. Castillo-Hernandez, N. Farahi, M. Yasseri, E. Mueller, J. de Boor, Mater. Today Energy. **21**, 100718 (2021)
10. D.C. Ramirez, L.R. Macario, X. Cheng, M. Cino, D. Walsh, Y.-C. Tseng, H. Kleinke, ACS Appl. Energy Mater. **3**, 2130 (2020)
11. G.K. Goyal, T. Dasgupta, Mater. Sci. Eng. B **272**, 115338 (2021)
12. N. Jia, J. Cao, X.Y. Tan, J. Dong, H. Liu, C.K.I. Tan, J. Xu, Q. Yan, X.J. Loh, A. Suwardi, Mater. Today Phys. **21**, 100519 (2021)
13. G.J. Snyder, E.S. Toberer, Nat. Mater. **7**, 105 (2008)
14. W. Luo, M. Yang, F. Chen, Q. Shen, H. Jiang, L. Zhang, Mater. Sci. Eng. B **157**, 96 (2009)
15. G. Jiang, J. He, T. Zhu, C. Fu, X. Liu, L. Hu, X. Zhao, Adv. Funct. Mater. **24**, 3776 (2014)
16. K. Kaur, R. Kumar, J. Electron. Mater. **46**, 4682 (2017)
17. P. Gao, X. Lu, I. Berkun, R.D. Schmidt, E.D. Case, T.P. Hogan, T.P. Hogan, Appl. Phys. Lett. **105**, 202104 (2014)
18. S.-M. Choi, T.H. An, W.-S. Seo, C. Park, I.-H. Kim, S.-U. Kim, J. Electron. Mater. **41**, 1071 (2012)
19. Y. Masuoka, Y. Mito, A. Ogino, T. Nakamura, K. Amano, R. Asahi, J. Alloys Compd. **781**, 606 (2019)

20. D. Shiojiri, T. Iida, H. Kakio, M. Yamaguchi, N. Hirayama, Y. Imai, J. Alloys Compd. **891**, 161968 (2022)
21. H. Kamila, G.K. Goyal, A. Sankhla, P. Ponnusamy, E. Mueller, T. Dasgupta, J. de Boor, Mater. Today Phys. **9**, 100133 (2019)
22. B.I. Rabiu, B. Huang, W.A. Shah, X. Luo, Y.Q. Yang, Chem. Phys. Lett. **823**, 140512 (2023)
23. G.K. Goyal, S. Mukherjee, R.C. Mallik, S. Vitta, I. Samajdar, T. Dasgupta, ACS Appl. Energy Mater. **2**, 2129 (2019)
24. J. Tani, H. Kido, Comput. Mater. Sci. **42**, 531 (2008)
25. H. Ma, D. Kim, S.I. Park, B.K. Choi, G. Park, H. Baek, H. Lee, H. Kim, J. Yu, W.C. Lee, J. Park, J. Yang, Adv. Sci. **10**, 2205690 (2023)
26. M. Yasseri, K. Mitra, A. Sankhla, J. de Boor, E. Müller, Acta Mater. **208**, 116737 (2021)
27. G.S. Polymeris, N. Vlachos, A.U. Khan, E. Hatzikraniotis, C.B. Lioutas, A. Delimitis, E. Pavlidou, Paraskevopoulos, and Th. Kyratsi. Acta Mater. **83**, 285 (2015)
28. S. Byeon, B. Wiendlocha, J. de Boor, K. Nielsch, H. Jin, J. Alloys Compd. **954**, 170157 (2023)
29. M. Cahana, H. Hayun, Y. Gelbstein, Phys. Chem. Chem. Phys. **24**, 21223 (2022)
30. W. Liu, H. Chi, H. Sun, Q. Zhang, K. Yin, X. Tang, Q. Zhang, C. Uher, Phys. Chem. Chem. Phys. **16**, 6893 (2014)
31. C.-H. Su, Mater. Today Phys. **5**, 58 (2018)
32. K. Yin, X. Su, Y. Yan, C. Uher, X. Tang, RSC Adv. **6**, 16824 (2016)
33. Y. Zheng, T.J. Slade, L. Hu, X.Y. Tan, Y. Luo, Z.-Z. Luo, J. Xu, Q. Yan, M.G. Kanatzidis, Chem. Soc. Rev. **50**, 9022 (2021)
34. N. Jia, X.Y. Tan, J. Xu, Q. Yan, M.G. Kanatzidis, Acc. Mater. Res. **3**, 237 (2022)
35. W. Liu, X. Tang, H. Li, K. Yin, J. Sharp, X. Zhou, C. Uher, J. Mater. Chem. **22**, 13653 (2012)